Research Article | Vol. 28, No. 11 / 25 May 2020 / Optics Express 16342
Optics EXPRESS

Sorting full angular momentum states with Pancharatnam-Berry metasurfaces based on spiral transformation

BAIMING WANG,[1,4] YUANHUI WEN,[1,4] JIANGBO ZHU,[2,3] YUJIE CHEN,[1,*] AND SIYUAN YU[1,2]

[1]State Key Laboratory of Optoelectronic Materials and Technologies, School of Electronics and Information Technology, Sun Yat-sen University, Guangzhou 510275, China
[2]Photonics Group, Merchant Venturers School of Engineering, University of Bristol, Bristol BS8 1UB, UK
[3]Department of Mathematics, Physics and Electrical Engineering, Northumbria University, Newcastle upon Tyne NE1 8ST, UK
[4]These authors contributed equally
[*]chenyj69@mail.sysu.edu.cn

Abstract: Full angular momentum states constitute a complete and higher state space of a photon, which are significant not only for fundamental study of light but also for practical applications utilizing cylindrical optics such as optical fibers. Here we propose and demonstrate a simple yet effective scheme of combining the spiral transformation with Pancharatnam-Berry (PB) metasurfaces for high-resolution sorting of full angular momentum states. The scheme is verified by successfully sorting full angular momentum states with 7 orbital angular momentum states and 2 spin angular momentum states via numerical simulations and experiments. We expect that our work paves the way for simple high-resolution sorting of full angular momentum states, which could be highly useful in both classical and quantum information systems.

1. Introduction

In both classical and quantum perspectives, the lightwave/photon has two kinds of angular momenta, including a spin angular momentum (SAM) and an orbital angular momentum (OAM). The SAM is associated with the circular polarization of light [1], and for its eigenstates $|\sigma\rangle$ each photon possesses an SAM of $S = \sigma\hbar$, where $\hbar$ is the reduced Planck constant and $\sigma = \pm 1$ corresponds to left- and right-handed circular polarizations, respectively. On the other hand, the OAM is associated with the helical wavefront of light [2], and for its eigenstates $|\ell\rangle$ each photon carries an OAM of $L = \ell\hbar$, where ℓ is the topological charge that can be any integer. The association of light's angular momentum states with its polarization and spatial structures is not only significant for the fundamental study, but also has important applications in various fields, such as high-capacity optical communications [3–7] and high-dimensional quantum information systems [8–12].

Precise sorting (also known as mode demultiplexing in optical communications) of these full angular momentum states is critical in the multi-state systems for the aforementioned applications. A simple yet efficient scheme is based on the optical coordinate transformation with a pair of Pancharatnam-Berry optical elements (PBOEs) [13], which is capable of simultaneously sorting SAM and OAM states with near unit efficiency even at the single-photon level. PBOEs are a kind of optical elements for wavefront shaping based on the PB phase, which is a geometric phase imposed by polarization conversion in contrast to a propagation phase [14,15]. Typical PBOEs include liquid-crystal devices [16] based on anisotropic-material birefringence and metallic or dielectric metasurfaces [17,18] based on structurally effective birefringence, among which the

#393859 https://doi.org/10.1364/OE.393859
Journal © 2020 Received 27 Mar 2020; revised 8 May 2020; accepted 11 May 2020; published 14 May 2020

Optics EXPRESS

PB dielectric metasurfaces are especially promising to form the PBOEs due to the advantages of simplified fabrication, high efficiency and strong manipulation of light.

Although the log-polar transformation is firstly and widely used for OAM sorting [19–22], its simplicity comes at the cost of an inherent limitation in the separation of adjacent OAM states, resulting in the need of an additional beam-copying technique [23–25] or a Mach-Zehnder interferometer [26] to alleviate this problem. Therefore, the following works in demonstration of simultaneously SAM and OAM sorting based on the log-polar transformation with PBOEs unavoidably suffer from the same aforementioned problem [16,27,28]. Recently, a new coordinate transformation called spiral transformation is proposed by the authors to realize high-resolution and efficient OAM sorting [29,30]. In this work, PB dielectric metasurfaces based on this spiral transformation are proposed and demonstrated for potential high-resolution sorting of full angular momentum states.

2. Design of PB metasurfaces with spiral transformation

The PB dielectric metasurface is a single-layer structure composed of an array of unit cells in sub-wavelength scale, which work as miniature half-wave plates with different local orientations [31,32]. The unit cell in the form of a cylinder can be considered as a Fabry-Pérot resonator and elliptic cross-section of the cylinder will lead to different effective refractive indices of light polarized along the two ellipse axes [31], resulting in structurally effective birefringence that can be utilized to design the unit cell working as a half-wave plate. For a PB metasurface composed of half-wave plates with spatially varying slow-axis orientations according to $\varphi(x, y)$, if circularly polarized light beams transmit through it, they will be converted into circularly polarized beams of opposite helicity and meanwhile imprinted with a PB phase of $\phi_L = 2\varphi(x, y)$ or $\phi_R = -2\varphi(x, y)$ for the input left- and right-handed circularly polarized light beams, respectively, resulting in polarization-dependent wavefront shaping.

In this work, our designed PB metasurface consists of a single-layer array of amorphous silicon elliptic cylinders standing on a quartz substrate and exposing in air as shown in Fig. 1(a). The refractive index of the amorphous silicon and the quartz substrate are $n_{\mathrm{Si}} = 3.5$ and $n_{\mathrm{q}} = 1.44$, respectively. The metasurface is formed by hexagonal lattice with a height of $H = 890$ nm and a lattice constant of $a = 850$ nm, namely $a_1 = a_2 = a$ as illustrated in Figs. 1(a) and 1(b). L_a and S_a represent the lengths of the long and short axes of the elliptic cylinder, respectively, and ϕ is the orientation angle of the long axis (or slow axis) of the elliptic cylinder with respect to the x-axis. In order to design the elliptic cylinder unit working as a miniature half-wave plate as required for forming PB metasurfaces, the parameters L_a and S_a of the elliptic cylinder are optimized by the finite-difference time-domain (FDTD) simulation for the working wavelength of 1550 nm. Through scanning the above parameters in simulation, the transmittance of the two incident light beams linearly polarized along the two ellipse axes and their phase difference are shown in Figs. 1(c)–1(e). Based on these results, $L_a = 495$ nm and $S_a = 305$ nm are selected for the elliptic cylinder to achieve a phase difference of π and high transmittance as required as well as in consideration of fabrication feasibility.

Based on the above PB metasurface design, the spiral coordinate transformation for sorting full angular momentum states can be implemented by a pair of PB phase metasurfaces, which work as an unwrapper and a phase corrector [29]. For a single-lens coordinate transformation system [33], the unwrapper and the phase corrector are located in the front and back focal planes of a lens denoted as (x, y) and (u, v), respectively. The phase modulation of the unwrapper is implemented by a PB metasurface with the slow-axis orientations described by

$$\phi_1(x, y) = A_0[(ax + y)\theta + (ay - x)\ln(\frac{r}{r_0}) - (ay - x)] + \frac{k\Delta u}{2d}x \tag{1}$$

Optics EXPRESS

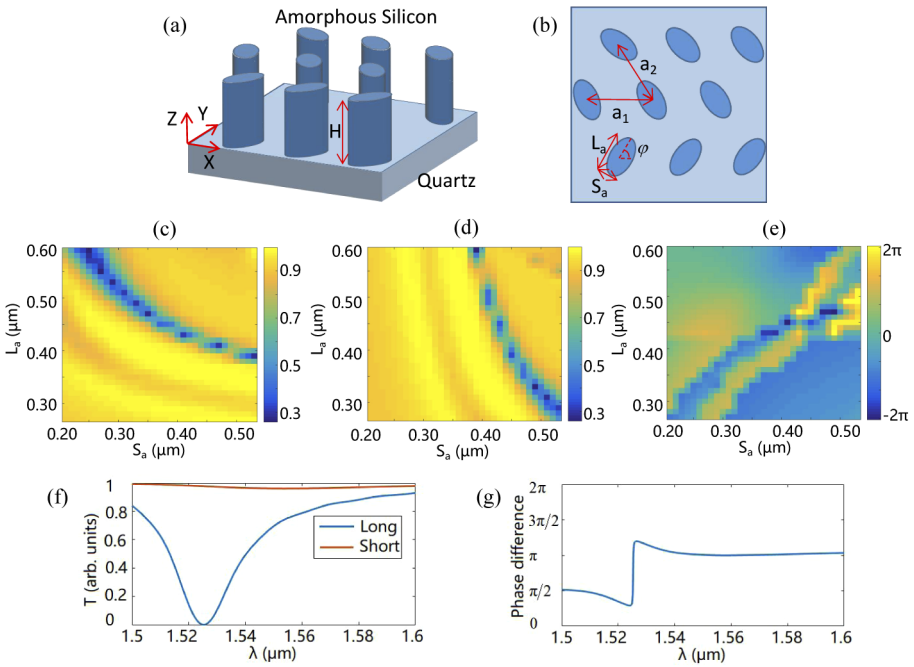

Fig. 1. Structures and simulation results of the designed PB dielectric metasurfaces. (a) Side and (b) top schematic views of the structure. (c),(d) Simulated maps of the transmittance as the functions of L_a and S_a for light beams linearly polarized along the long and short axes, respectively. The colorbar represents the normalized value. (e) Simulated map of the phase difference between the two light beams. (f),(g) Transmittances and the phase difference for the two orthogonal polarized light beams after passing through the elliptic cylinder with L_a = 495 nm and S_a = 305 nm, respectively.

where $A_0 = k\beta / \left[2d(1+a^2)\right]$ for brevity, k is the wavenumber in free space and d is the focal length of the intermediate lens. (r, θ) are polar coordinates describing spirals by $r = f(\theta) = s\exp(a\theta)$ (different values of s represent different spirals in the plane) in the spiral transformation, with the polar angle θ not necessarily limited to a 2π range. β, r_0 and a are the scaling parameters of the spiral transformation, and Δu>0 is a lateral shifting parameter for separating the two SAM states in the plane (u, v).

After passing through the PB unwrapper, the incident SAM-OAM state with an annular intensity distribution will be unwrapped to a transformed beam with a long stripe-shaped profile, and the transformed beams for the two orthogonal SAM states are centrosymmetric around the origin. Note that the transformed beams not only contain the desired linear phase gradient mapped from the azimuthal phase gradient of the OAM state that is useful for OAM sorting, but also have a phase distortion resulting from the phase modulation by the unwrapper and the phase acquired during propagation between planes (x, y) and (u, v). Therefore, a phase corrector in the output plane (u, v) is required for phase compensation. As the transformed beams for the two SAM states are separated in the plane (u, v) by $\pm\Delta u$, they can be phase-corrected in each half-plane respectively, implemented by a PB phase corrector with the slow-axis orientations

Optics EXPRESS

described by

$$\begin{cases} \phi_{2L}(u,v) = -A_0 r_0 \exp\left[\dfrac{av-(u-\Delta u)}{\beta}\right]\cdot(-\cos B + a\sin B) - \dfrac{ku\Delta m}{2f} \\ \phi_{2R}(u,v) = -A_0 r_0 \exp\left[\dfrac{av-(u+\Delta u)}{-\beta}\right]\cdot(-\cos C + a\sin C) - \dfrac{ku\Delta m}{2f} \end{cases} \tag{2}$$

where the subscript L and R correspond to the half planes of u>0 and u<0, respectively. $B = [a(u-\Delta u)+v)]/\beta$, and $C = [a(-u-\Delta u)-v)]/\beta$ for brevity. f is the focal length of a lens finally used to separate full angular momentum states in its focal plane (m,n), and $\pm\Delta m$ are the lateral locations of the two SAM states. After passing through the PB phase corrector, the SAM-OAM states are transformed into planewaves with different linear phase gradients or tilted angles, which are eventually focused to correspondingly different positions in the focal plane (m,n) of a lens given by

$$(m,n) = \left[\left(\Delta m + \frac{af}{k\beta}\ell\right)\sigma, \frac{f}{k\beta}\ell\sigma\right] \tag{3}$$

Since the parameter a describes the growth rate of the spiral and typically has a<<1 in order to ensure multiple spiral turns within the input wavefront, the lateral and vertical positions are thus mainly determined by the SAM state and the OAM state, respectively. The SAM state will also determine whether there is an inversed mapping along the vertical direction. For demonstration, typical values of the parameters including $k = 2\pi/\lambda = 2\pi/(1.550\ \mu\text{m})$, $d = 25.4$ mm, $r_0 = 800\ \mu$m, $\beta = 1200\ \mu\text{m}/(2\pi)$, $a = \ln(1.4)/(2\pi)$, $\Delta u = 500\ \mu$m, $\Delta m = 2500\ \mu$m, and $f = 100$ mm are used in our design, with which the slow-axis orientation angle distributions of the PB unwrapper and the PB phase corrector are shown in Fig. 2.

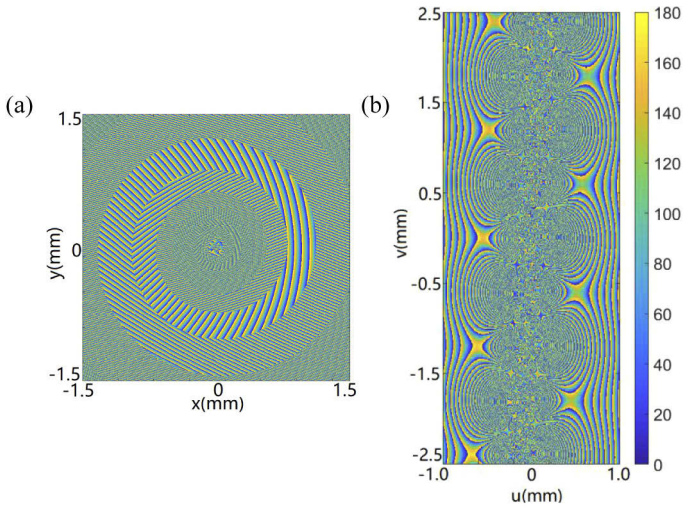

Fig. 2. Slow-axis orientation angle distributions of the designed PB metasurfaces for (a) the unwrapper, and (b) the phase corrector. The unit of the colorbar is degrees.

The designed metasurfaces are fabricated according to the fabrication process illustrated in Fig. 3(a). The inductively coupled plasma-chemical vapor deposition (ICP-CVD) is firstly used to deposit an 890-nm-thick amorphous silicon film on a 1-mm-thick quartz substrate. After deposition, a 500-nm thick negative resist of hydrogen silsesquioxane (HSQ) is spin-coated on the amorphous silicon and then a thin aluminum film is sputtered for enhancement of conductivity. The PB metasurface pattern is defined in the resist by electron beam lithography (EBL). After

Optics EXPRESS

that, the aluminum film is removed with H_3PO_4 (5% in H_2O) at 50 °C for 5-10 minutes, while the HSQ film is developed in the methyl isobutyl ketone (MIBK) for 90 seconds. The pattern in the HSQ resist is then transferred to the amorphous silicon film by inductively coupled plasma (ICP) etching. Finally, the residual HSQ resist is removed by HF (10% in H_2O) for 10 seconds, and hence the amorphous silicon PB metasurface on a quartz substrate is finally obtained, as shown in Figs. 3(b)–3(d).

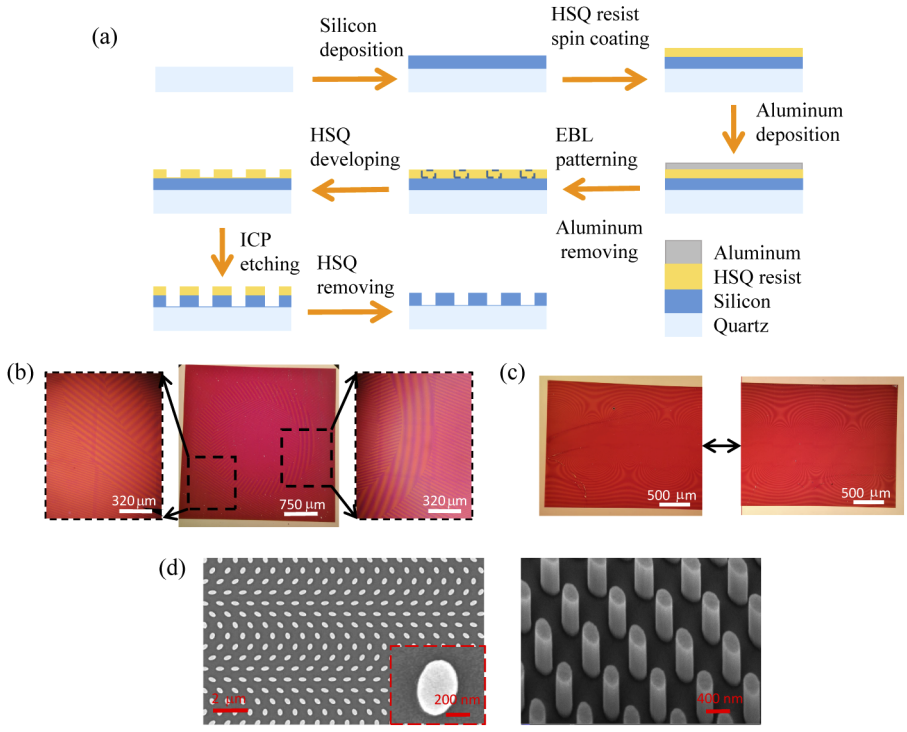

Fig. 3. Fabrication of the full angular momentum sorter consisting of the PB unwrapper and the PB phase corrector. (a) Schematic of the fabrication process. The dotted boxes represent the unexposed area. (b),(c) Optical microscope images of (b) the unwrapper and (c) the phase corrector. Because of the limited field of view in the optical microscope, the phase corrector is divided into two parts, with the left and right parts corresponding to the top and bottom parts in Fig. 2(b) respectively. (d) Scanning electron microscopy images of the unwrapper for a view of the amorphous silicon nano-cylinders within the PB metasurface.

3. Optical characterization and results

Based on the fabricated PB metasurfaces as the unwrapper and the phase corrector, an optical setup for full angular momentum state measurement is built and illustrated in Fig. 4. A laser operating at the wavelength $\lambda = 1550$ nm emits a linearly polarized (LP) Gaussian beam. After both amplitude and phase modulations by a spatial light modulator (SLM) in a 4f system consisting of lens1 and lens2, a perfect vortex beam [34] with different OAM states is generated while the SAM state is determined by the orientation of the quarter-wave plate. For demonstration of simultaneously sorting of both SAM and OAM states, an LP state regarded as the superposed SAM states of $\sigma = \pm 1$ and OAM states with $\ell = 0, \pm 1, \pm 2, \pm 3$ are employed.

The incident angular momentum beams after passing through the PB unwrapper, Lens2 and PB phase corrector are transformed to stripe-shaped beams as shown in Fig. 5. The experimental

Optics EXPRESS

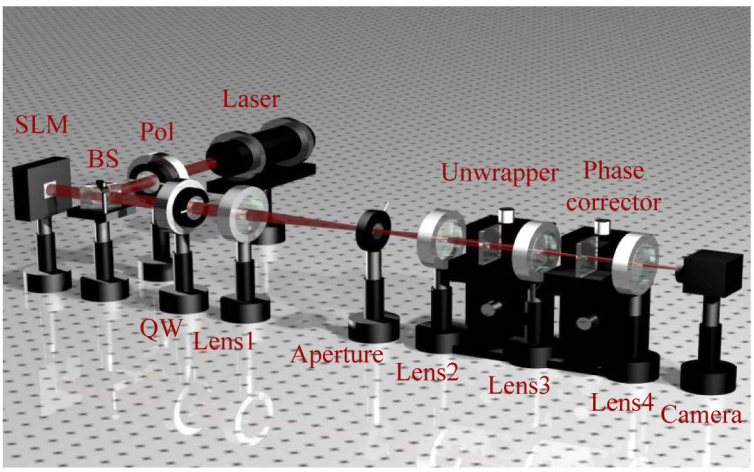

Fig. 4. Schematic of the experimental setup for optical characterization. Pol: linear polarizer; BS: beam splitter; SLM: spatial light modulator; QW: quarter-wave plate; The focal lengths of Lens 1-4 are $f_1 = 200$ mm, $f_2 = 100$ mm, $f_3 = d = 25.4$ mm, and $f_4 = f = 100$ mm, respectively.

results match well with the numerical simulations including the separation between the two SAM states and the stripe shape of the transform beams. Note that there is a slight displacement along the vertical direction between the experimental result and the simulation, which is attributed to the slightly discrepant size of the incident beams. It is also noted that a light spot appears in the center resulting from the imperfect phase modulation by the PB unwrapper. After the final Fourier transform implemented by the lens4, these transformed beams corresponding to different angular momentum states are focused to different positions in the focal plane according to Eq. (3),

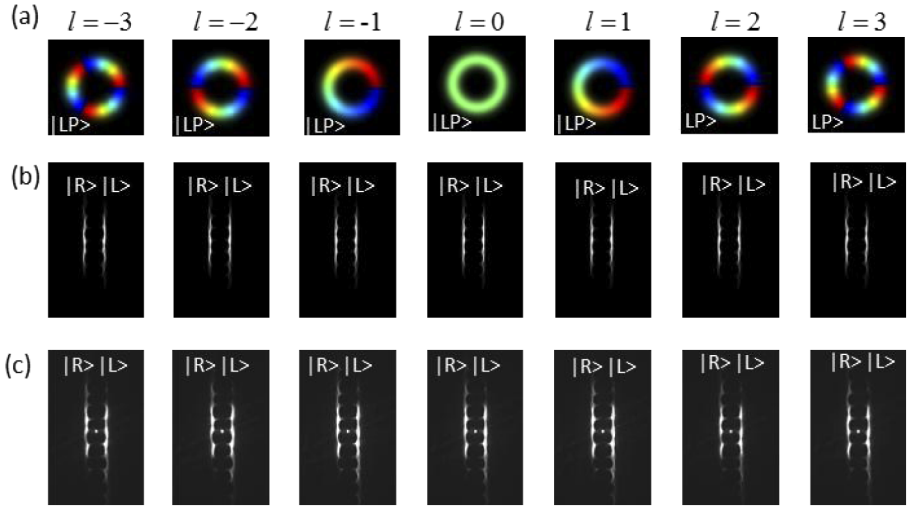

Fig. 5. Incident SAM-OAM light beams and the correspondingly transformed beams after the spiral transformation. (a) Complex field distributions of the incident SAM-OAM states in the input plane (x, y). (b),(c) Transformed beams in the output plane (u, v) after the spiral transformation (b) in simulation and (c) in experiment.

Optics EXPRESS

which are recorded by an infrared camera. The intensity distributions of the sorted beam for each input state are summarized in Fig. 6. It is shown that two SAM states are located in different lateral position m with a spacing of $2 \cdot (\Delta m) = 5$ mm as expected. Moreover, different OAM states are located in different vertical positions proportional to the ℓ value, and the position $-\ell$ mapping correlations are opposite for the two SAM states, as predicted by Eq. (3).

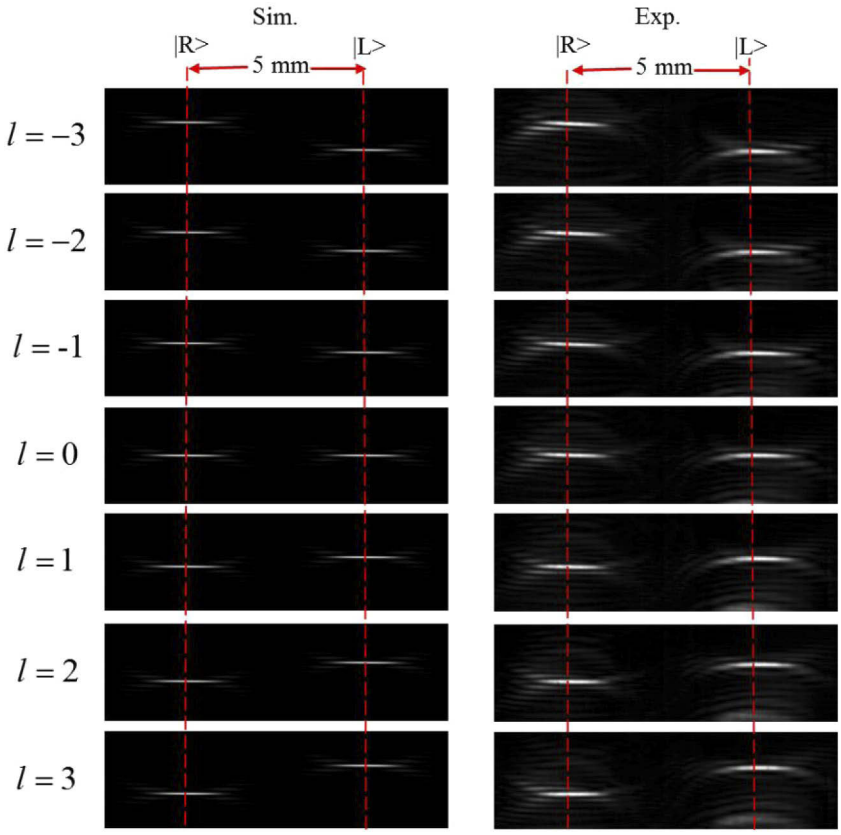

Fig. 6. Sorted beams in the focal plane (m, n) of the lens corresponding to different full angular momentum states including 7 OAM states ($-3 \leq \ell \leq 3$) and 2 SAM states ($|L\rangle$, $|R\rangle$). Simulated (Sim.) and experimental (Exp.) results are summarized and all the images are in the same scale for easier comparison. The intensity profiles along the red dashed lines are presented in Fig. 7.

For a quantitative analysis of sorting OAM states, the corresponding intensity profiles along the middle vertical lines in Fig. 6 are drawn and presented in Fig. 7. It is shown that the located positions of each angular momentum state coincide precisely between the simulation and the experiment, with the spatial distance between adjacent modes close to the theoretical value of $f/(k\beta) = 100000 \times 1.55/1200\ \mu\text{m} \approx 129\ \mu\text{m}$. However, it is also noted that the obtained sorted beams are broadened in the experiment compared to the simulation and have some stray lights in the background, resulting in the increase of the crosstalk between adjacent OAM states. In order to quantify the separation of different OAM states, a concept of optical finesse, defined as the ratio of the spacing between neighboring OAM states over their average full width half maximum (FWHM), can be exploited [25]. For the designed and fabricated sorter, this indicator is calculated as 2.63 for the two SAM states in the simulation, while it decrease to 1.18 and 1.05 for σ = -1 and σ = +1 in the experiment, respectively. The non-ideal results can be attributed

Optics EXPRESS

to the imperfect phase modulation as indicated by the central light spot in Fig. 5 and the slight misalignment between the unwrapper and the phase corrector in the measurement, which could be further improved with optimized nanofabrication techniques and integration of the two elements as a whole [30,35,36]. The insertion loss of the SAM-OAM sorter is also measured to be 3.5 dB and 2.9 dB for input left- and right-circular polarized light, respectively.

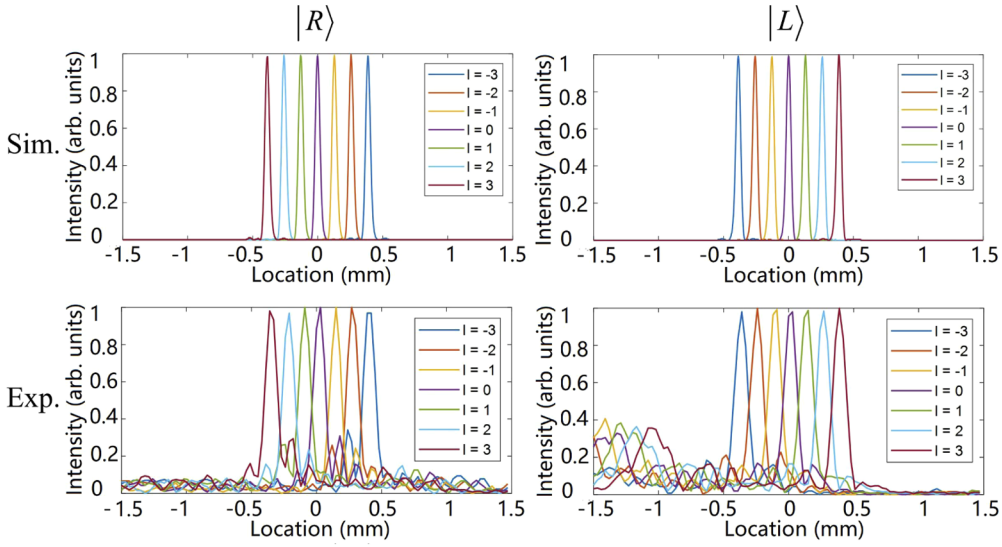

Fig. 7. Intensity profiles along the red dashed lines marked in Fig. 6, including simulated (Sim.) and experimental (Exp.) results for right-handed and left-handed circularly polarized states, respectively.

4. Conclusion

A scheme for sorting full angular momentum states is proposed and experimentally verified, which harnesses the capability of SAM sorting based on PB metasurfaces with high-resolution OAM sorting based on the spiral coordinate transformation. Full angular momentum states including seven OAM states ($-3 \leq \ell \leq 3$) and two SAM states ($\sigma = \pm 1$) are successfully sorted into corresponding positions in space as predicted by the theory, with experimental results matching well with the numerical simulations. We anticipate that the proposed scheme will not only extend the original sorting of OAM states enabled by the spiral transformation to a more general sorting of full angular momentum states, but also find important applications in both classical and quantum information systems based on joint SAM-OAM multiplexing and encoding.

Funding

National Key R&D Program of China (2019YFA0706302; 2018YFB1801800); National Natural Science Foundation of China (NSFC) (U1701661, 11774437); Local Innovative and Research Teams Project of Guangdong Pearl River Talents Program (2017BT01X121); Science and Technology Program of Guangzhou (201804010302).

Disclosures

The authors declare no conflicts of interest.

Optics EXPRESS

References

1. J. H. Poynting, "The wave motion of a revolving shaft, and a suggestion as to the angular momentum in a beam of circularly polarised light," Proc. R. Soc. Lond. A **82**(557), 560–567 (1909).
2. L. Allen, M. W. Beijersbergen, R. Spreeuw, and J. Woerdman, "Orbital angular momentum of light and the transformation of laguerre-gaussian laser modes," Phys. Rev. A **45**(11), 8185–8189 (1992).
3. G. Gibson, J. Courtial, M. J. Padgett, M. Vasnetsov, V. Pas'ko, S. M. Barnett, and S. Franke-Arnold, "Free-space information transfer using light beams carrying orbital angular momentum," Opt. Express **12**(22), 5448–5456 (2004).
4. J. Wang, J.-Y. Yang, I. M. Fazal, N. Ahmed, Y. Yan, H. Huang, Y. Ren, Y. Yue, S. Dolinar, M. Tur, and A. E. Willner, "Terabit free-space data transmission employing orbital angular momentum multiplexing," Nat. Photonics **6**(7), 488–496 (2012).
5. N. Bozinovic, Y. Yue, Y. Ren, M. Tur, P. Kristensen, H. Huang, A. E. Willner, and S. Ramachandran, "Terabit-scale orbital angular momentum mode division multiplexing in fibers," Science **340**(6140), 1545–1548 (2013).
6. G. Zhu, Z. Hu, X. Wu, C. Du, W. Luo, Y. Chen, X. Cai, J. Liu, J. Zhu, and S. Yu, "Scalable mode division multiplexed transmission over a 10-km ring-core fiber using high-order orbital angular momentum modes," Opt. Express **26**(2), 594–604 (2018).
7. J. Liu, G. Zhu, J. Zhang, Y. Wen, X. Wu, Y. Zhang, Y. Chen, X. Cai, Z. Li, Z. Hu, J. Zhu, and S. Yu, "Mode division multiplexing based on ring core optical fibers," IEEE J. Quantum Electron. **54**(3), 1 (2018).
8. A. Mair, A. Vaziri, G. Weihs, and A. Zeilinger, "Entanglement of the orbital angular momentum states of photons," Nature **412**(6844), 313–316 (2001).
9. M. Bourennane, A. Karlsson, G. Björk, N. Gisin, and N. J. Cerf, "Quantum key distribution using multilevel encoding: security analysis," J. Phys. A: Math. Gen. **35**(47), 10065–10076 (2002).
10. S. Gröblacher, T. Jennewein, A. Vaziri, G. Weihs, and A. Zeilinger, "Experimental quantum cryptography with qutrits," New J. Phys. **8**(5), 75 (2006).
11. M. Mirhosseini, O. S. Magaña-Loaiza, M. N. O'Sullivan, B. Rodenburg, M. Malik, M. P. Lavery, M. J. Padgett, D. J. Gauthier, and R. W. Boyd, "High-dimensional quantum cryptography with twisted light," New J. Phys. **17**(3), 033033 (2015).
12. A. Sit, F. Bouchard, R. Fickler, J. Gagnon-Bischoff, H. Larocque, K. Heshami, D. Elser, C. Peuntinger, K. Günthner, B. Heim, C. Marquardt, G. Leuchs, R. W. Boyd, and E. Karimi, "High-dimensional intracity quantum cryptography with structured photons," Optica **4**(9), 1006–1010 (2017).
13. G. F. Walsh, "Pancharatnam-Berry optical element sorter of full angular momentum eigenstate," Opt. Express **24**(6), 6689–6704 (2016).
14. S. Pancharatnam, "Generalized theory of interference and its applications," in *Proceedings of the Indian Academy of Sciences-Section A*, vol. 44 (Springer, 1956), pp. 398–417.
15. M. V. Berry, "The adiabatic phase and pancharatnam's phase for polarized light," J. Mod. Opt. **34**(11), 1401–1407 (1987).
16. H. Larocque, J. Gagnon-Bischoff, D. Mortimer, Y. Zhang, F. Bouchard, J. Upham, V. Grillo, R. W. Boyd, and E. Karimi, "Generalized optical angular momentum sorter and its application to high-dimensional quantum cryptography," Opt. Express **25**(17), 19832–19843 (2017).
17. X. Zhao, X. Feng, F. Liu, K. Cui, W. Zhang, and Y. Huang, "A compound phase-modulated beam splitter to distinguish both spin and orbital angular momentum," ACS Photonics **7**(1), 212–220 (2020).
18. G. Ruffato, P. Capaldo, M. Massari, E. Mafakheri, and F. Romanato, "Total angular momentum sorting in the telecom infrared with silicon Pancharatnam-Berry transformation optics," Opt. Express **27**(11), 15750–15764 (2019).
19. G. C. Berkhout, M. P. Lavery, J. Courtial, M. W. Beijersbergen, and M. J. Padgett, "Efficient sorting of orbital angular momentum states of light," Phys. Rev. Lett. **105**(15), 153601 (2010).
20. M. P. Lavery, D. J. Robertson, G. C. Berkhout, G. D. Love, M. J. Padgett, and J. Courtial, "Refractive elements for the measurement of the orbital angular momentum of a single photon," Opt. Express **20**(3), 2110–2115 (2012).
21. G. Ruffato, M. Massari, and F. Romanato, "Compact sorting of optical vortices by means of diffractive transformation optics," Opt. Lett. **42**(3), 551–554 (2017).
22. S. Lightman, G. Hurvitz, R. Gvishi, and A. Arie, "Miniature wide-spectrum mode sorter for vortex beams produced by 3D laser printing," Optica **4**(6), 605–610 (2017).
23. M. N. O'Sullivan, M. Mirhosseini, M. Malik, and R. W. Boyd, "Near-perfect sorting of orbital angular momentum and angular position states of light," Opt. Express **20**(22), 24444–24449 (2012).
24. M. Mirhosseini, M. Malik, Z. Shi, and R. W. Boyd, "Efficient separation of the orbital angular momentum eigenstates of light," Nat. Commun. **4**(1), 2781 (2013).
25. C. Wan, J. Chen, and Q. Zhan, "Compact and high-resolution optical orbital angular momentum sorter," APL Photonics **2**(3), 031302 (2017).
26. Z. Feng, X. Wang, M. I. Dedo, K. Guo, F. Shen, C. Kai, and Z. Guo, "High-density orbital angular momentum mode analyzer based on the mode converters combining with the modified Mach–Zehnder interferometer," Opt. Commun. **435**, 441–448 (2019).
27. G. F. Walsh, L. De Sio, D. E. Roberts, N. Tabiryan, F. J. Aranda, and B. R. Kimball, "Parallel sorting of orbital and spin angular momenta of light in a record large number of channels," Opt. Lett. **43**(10), 2256–2259 (2018).

Optics EXPRESS

28. S. Zheng, Y. Li, Q. Lin, X. Zeng, G. Zheng, Y. Cai, Z. Chen, S. Xu, and D. Fan, "Experimental realization to efficiently sort vector beams by polarization topological charge via Pancharatnam–Berry phase modulation," Photonics Res. **6**(5), 385–389 (2018).
29. Y. Wen, I. Chremmos, Y. Chen, J. Zhu, Y. Zhang, and S. Yu, "Spiral transformation for high-resolution and efficient sorting of optical vortex modes," Phys. Rev. Lett. **120**(19), 193904 (2018).
30. Y. Wen, I. Chremmos, Y. Chen, G. Zhu, J. Zhang, J. Zhu, Y. Zhang, J. Liu, and S. Yu, "Compact and high-performance vortex mode sorter for multi-dimensional multiplexed fiber communication systems," Optica **7**(3), 254–262 (2020).
31. A. Arbabi, Y. Horie, M. Bagheri, and A. Faraon, "Dielectric metasurfaces for complete control of phase and polarization with subwavelength spatial resolution and high transmission," Nat. Nanotechnol. **10**(11), 937–943 (2015).
32. D. Lin, P. Fan, E. Hasman, and M. L. Brongersma, "Dielectric gradient metasurface optical elements," Science **345**(6194), 298–302 (2014).
33. W. Hossack, A. Darling, and A. Dahdouh, "Coordinate transformations with multiple computer-generated optical elements," J. Mod. Opt. **34**(9), 1235–1250 (1987).
34. A. S. Ostrovsky, C. Rickenstorff-Parrao, and V. Arrizón, "Generation of the "perfect" optical vortex using a liquid-crystal spatial light modulator," Opt. Lett. **38**(4), 534–536 (2013).
35. G. Ruffato, M. Massari, M. Girardi, G. Parisi, M. Zontini, and F. Romanato, "Non-paraxial design and fabrication of a compact OAM sorter in the telecom infrared," Opt. Express **27**(17), 24123–24134 (2019).
36. Y. Wen, J. Zhu, Y. Chen, L. Zhou, L. Liu, C. Yang, Y. Zhang, and S. Yu, "Cascaded metasurface structures," in *2017 Conference on Lasers and Electro-Optics Pacific Rim*, (Optical Society of America, 2017), p. s1778.